


Letter

Evaluation of the Diurnal Variation of Upper Tropospheric Humidity in Reanalysis Using Homogenized Observed Radiances from International Geostationary Weather Satellites

Yunheng Xue ^{1,2,3} , Jun Li ^{2,*}, Zhenglong Li ², Mathew M. Gunshor ² and Timothy J. Schmit ⁴

¹ Institute of Atmospheric Physics, Chinese Academy of Sciences, Beijing 100029, China; yxue44@wisc.edu

² Cooperative Institute for Meteorological Satellite Studies, University of Wisconsin-Madison, Madison, WI 53705, USA; zli@ssec.wisc.edu (Z.L.); matg@ssec.wisc.edu (M.M.G.)

³ University of Chinese Academy of Sciences, Beijing 100029, China

⁴ Center for Satellite Applications and Research, CoRP/ASPB, Madison, WI 53705, USA; tim.j.schmit@noaa.gov

* Correspondence: jun.li@ssec.wisc.edu

Received: 16 April 2020; Accepted: 18 May 2020; Published: 19 May 2020



Abstract: A near global dataset of homogenized clear-sky 6.5- μm brightness temperatures (BTs) from international geostationary (GEO) weather satellites has recently been generated and validated. In this study, these radiance measurements are used to construct the diurnal variation of upper tropospheric humidity (UTH) and to evaluate these diurnal variations simulated by five reanalysis datasets over the 45° N–45° S region. The features of the diurnal variation described by the new dataset are comparable with previous observational studies that a land–sea contrast in the diurnal variation of UTH is exhibited. Distinct diurnal variations are observed over the deep convective regions where high UTH exists. The evaluation of reanalysis datasets indicates that reanalysis systems still have considerable difficulties in capturing the observed features of the diurnal variation of UTH. All five reanalysis datasets present the largest wet biases in the afternoon when the observed UTH experiences a diurnal minimum. Reanalysis can roughly reproduce the day–night contrast of UTH but with much weaker amplitudes and later peak time over both land and ocean. Comparison of the geographical distribution of the diurnal variation shows that both ERA5 and MERRA-2 could capture the larger diurnal variations over convective regions. However, the diurnal amplitudes are widely underestimated, especially over convective land regions, while the phase biases are relatively larger over open oceans. These results suggest that some deficiencies may exist in convection and cloud parameterization schemes in reanalysis models.

Keywords: diurnal variation; upper tropospheric humidity; homogenized radiances; GEO weather satellites; evaluation of reanalysis

1. Introduction

Atmospheric water vapor (WV) is one of the major absorption gases of the outgoing longwave radiation. Although the WV content decreases with altitude rapidly, the outgoing longwave radiation (OLR) at the top of the atmosphere (TOA) is more sensitive to the upper tropospheric WV, and even small variations in upper tropospheric humidity (UTH) may lead to a significant impact on the radiation energy budget and climate feedback [1–4]. However, UTH is one of the least well-monitored atmospheric variables due to its high variability in both space and time and the lack of accurate conventional observations in the upper troposphere [5–7].

The reanalysis datasets are widely used to monitor and project the variability of key climate variables and must be continuously assessed to understand their strengths and weaknesses [8–10]. Previous studies have indicated that reanalysis has difficulties to accurately simulate the WV above the tropopause [9–11]. Valid observations for assimilation in the upper troposphere are sparse, and thus reanalysis data heavily rely on the “first guess” from their host models [12]. Given the importance of the UTH for radiative forcing, the uncertainties of UTH may lead to misrepresentations in radiative and dynamical processes in reanalysis. The diurnal variation is one of the most fundamental modes in the climate system. Simulations of diurnal variations of atmospheric variables are one important check of the reliability of a reanalysis system [13]. Some studies [14–16] have suggested that the deficiencies in simulating diurnal variation of UTH can help further identify the potential problems in convection and cloud parameterization in reanalysis systems. Therefore, it is important to assess how well reanalysis data capture the observed diurnal variability of UTH.

Geostationary (GEO) weather satellites monitor infrared (IR) radiation at the WV absorption bands with high spatiotemporal resolution and large spatial coverage. It was shown that the clear sky near 6.7- μm WV brightness temperature at nadir view is linearly related to the natural logarithm of UTH [17] based on simplified radiative theory and certain assumptions of atmospheric profiles:

$$\ln UTH = a + bT_{6.7clr}, \quad (1)$$

where a (~ 31.5) and b (~ -0.1) can be treated as nearly constant values for interpretation purposes. This simplified equation demonstrates that, to a reasonable degree of accuracy, the near 6.7- μm WV absorption spectral region radiances can be interpreted in terms of a more familiar water vapor measurements, i.e., UTH. The UTH is defined as the mean relative humidity averaged over a broad layer between approximately 200 and 500 hPa, indicated by the moisture Jacobian function of the near 6.7- μm WV band [18,19]. As a result, the WV radiances from GEO weather satellites have been widely used for studying the diurnal variation of UTH [11,14,15,17]. Studies have found that the diurnal cycle of UTH has a land–sea contrast with larger amplitude and later peak time over land than over the oceans [14–16]. The diurnal variation of UTH usually lags deep convection and high clouds, indicating the importance of deep convection in moistening the upper troposphere through the evaporation/sublimation of the clouds [15]. Scientists have also tried to validate the diurnal characteristics of UTH in climate models and reanalysis datasets. For example, the simulation of UTH in two climate models are compared with microwave and IR measurements from polar orbiting satellites over selected convective regions [20]. The diurnal variation of UTH in five reanalysis datasets over the convectively active regions of Africa and the Atlantic Ocean has been evaluated with 6.7- μm WV band radiances from Meteosat-5 [11]. However, these studies have usually been limited to polar orbiting satellites that have large temporal gaps or limited to a single GEO satellite due to the spectral differences among international GEO weather satellites.

Recently, a new homogenized IR 6.5- μm WV absorption band radiance dataset (referred to as homogenized WV radiances data hereafter) from multiple international GEO weather satellites has been successfully generated [19]. This homogenized WV radiances dataset maintains the high spatial and temporal resolution of GEO satellites and has near global coverage of the tropics and mid-latitudes. It provides a great opportunity to perform a near global assessment of diurnal variation of UTH in reanalysis datasets.

The purpose of this study is to construct the diurnal variation of UTH with the homogenized WV radiance data on a near global scale. This dataset will then be further used to evaluate the capability of five reanalysis datasets to capture these observed diurnal variations. The paper is organized as follows: the homogenized WV radiance data, reanalysis simulations, and diurnal analysis method are described in Section 2. The main results of the observed diurnal variation of UTH from GEO weather satellites and the evaluation of the five different reanalysis datasets are given in Section 3. Section 4 presents the discussion, while the conclusions are in Section 5.

2. Data and Methodologies

2.1. Homogenized WV Radiances from International GEO Weather Satellites

The homogenized WV radiances (expressed as equivalent brightness temperatures, or BTs) data were generated by homogenizing seven international GEO weather satellite imagers' WV radiances (see Table 1 in Li et al. [19]) to the nadir view radiances of GOES-15 Imager 6.5- μm WV band. The homogenization process accounts for both spectral differences and the limb (angle) effect between other GEO imagers and GOES-15 Imager. The cloud detection process is based on a simple cloud mask scheme in post-processing to remove the contaminations by high clouds. The accuracies of the homogenized clear sky WV radiances data have been validated with the independent hyperspectral sounder [21] Infrared Atmospheric Sounding Interferometer (IASI) radiances from both Metop-A and Metop-B. This 3-hourly observation archive covers the years from 2015 to 2017 with the spatial coverage of 45° N–45° S and all longitudes. The reader is referred to Li et al. [19] for detailed technical approaches on this dataset.

2.2. Reanalysis Datasets

Recently, the quality of modern reanalysis systems has been much improved due to the great efforts made in forecast models and data assimilation (DA) systems [22–24]. In this study, five reanalysis datasets were evaluated. They were the European Centre for Medium-Range Weather Forecasts' (ECMWF) newly released fifth generation reanalysis (ERA5, [25]), the ECMWF Interim Reanalysis (ERA-Interim, [22]), the National Centers for Environmental Prediction's (NCEP) Climate Forecast System reanalysis, version 2 (CFSv2, [26], which is also referred to as CFSR), the Modern-Era Retrospective Analysis for Research and Applications version 2 (MERRA-2, [24]), and the 55-year modern Japanese Reanalysis Projects (JRA55, [23]). Some of the basic information of the five reanalysis datasets is listed in Table 1. It should be noted that the temporal interval is 6 h for ERA-Interim, CFSR and JRA-55, while ERA5 and MERRA-2 can provide 3-hourly meteorological variables, which is consistent with the homogenized WV radiances.

Table 1. Basic characteristics of reanalysis datasets evaluated. IFS: Integrated Forecasting System. GEOS: Goddard Earth Observing System Model developed by the National Aeronautics and Space Administration (NASA)'s Global Modeling and Assimilation Office (GMAO). CFS: The National Centers for Environmental Prediction's (NCEP) Climate Forecast System. GSM: Global Spectral Model of the Japan Meteorological Agency (JMA).

Reanalysis	ERA5	ERA-Interim	CFSR	MERRA-2	JRA-55
Source	ECMWF	ECMWF	NCEP	NASA GMAO	JMA
Forecast Model	IFS Cycle 41r2	IFS Cycle 31r2	CFS	GEOS 5.12.4	JMA GSM
Assimilation Scheme	4D-VAR	4D-VAR	3D-VAR	3D-VAR	4D-VAR
Vertical Resolution (Pressure Level)	37	37	37	42	37; 27 for WV profiles
Horizontal Resolution	0.25° × 0.25°	0.75° × 0.75°	0.5° × 0.5°	0.5° × 0.625°	1.25° × 1.25°
Temporal Resolution	1 hourly	6 hourly	6 hourly	3 hourly	6 hourly

2.3. Methodologies

The evaluation in this study was based on the WV radiances rather than the WV retrievals. A profile-to-radiance approach [11,12,27] was adopted. Atmospheric profiles of temperature and humidity from reanalysis datasets were input with surface information into the Community Radiative Transfer Model (CRTM) v2.1.3 [28] using Optical Depth in Pressure Space (ODPS) coefficients to simulate the clear-sky GOES-15 Imager 6.5- μm WV band BTs at nadir view. Many studies [29–31] have validated the CRTM capability of simulating IR radiances with the rigorous line-by-line radiative transfer model (LBLRTM) [32]. The LBLRTM provides spectral radiance calculations with high

accuracies and is widely regarded as a standard benchmark for RTM model evaluations. It was shown that both the bias and root-mean-square error of CRTM are mostly below 0.15 K, indicating that the CRTM is quite accurate for clear sky IR radiance simulations. Therefore, the large differences between observed radiances and simulated radiances could be mainly attributed to the deficiencies in reanalysis datasets, which can then be interpreted to the UTH uncertainties based on Equation (1). The cloud mask from observations was used for reanalysis to exclude the grids that may contain the cloud contamination in reanalysis and to ensure the reanalysis simulations have the same sampling gaps as observations. All the data, including the observations and the reanalysis simulations, were then re-gridded to a $0.5^\circ \times 0.5^\circ$ horizontal grid format using an inverse distance squared weighted interpolation method.

To characterize the main signal of the periodically repeated diurnal signal and reduce the weather noise, a “composite day” was necessary to be first prepared by averaging the BT fields at each time step for a given period at each grid. The Fourier decomposition of 3-hourly diurnal cycle composites are widely used in diurnal analysis [2,15,16,33–36]. A first-order Fourier series was fitted to the daily composite to estimate the amplitude and phase of the BT diurnal variation for each $0.5^\circ \times 0.5^\circ$ grid box:

$$BT(t) = \overline{BT} + A \cos\left[\frac{2\pi}{24}(t - P)\right] + residual, \quad (2)$$

where \overline{BT} is the diurnal mean, t is the local solar time (LST) in hours, A represents the amplitude of the BTs, and P represents the diurnal phase of BTs. It should be noted that the diurnal phase of BTs corresponds to the LST showing maximum value of BTs. Since there is a strong negative correlation (-0.968) between the BT and the corresponding value of the $\ln UTH$ [17], the diurnal variation of BT can be easily interpreted to the diurnal variation of UTH. A large amplitude of BTs represents a large diurnal amplitude of UTH, and the LST for maximum UTH (referred to as the phase of UTH hereafter) corresponds to the LST showing the minimum value of BT, which is denoted by $P + 12$ in Equation (2). The diurnal amplitude of BTs and the phase of UTH will then be displayed in vector maps (Figures 2 and 5) to highlight the geographical distribution of the diurnal variation of UTH.

The Fisher statistical significance test (F-test) was used to determine the statistical significance [33,37] of the Fourier first harmonic fit. The results are only shown where the first harmonic fit is statistically significant at the 90% confidence level [37] in all vector figures.

3. Results

3.1. Characteristics of Observed Diurnal Variation

3.1.1. Observed Diurnal Anomaly

The diurnal anomaly is calculated by the daily composite at a given time minus the daily mean. The diurnal anomalies of the area-weighted average of observed $6.5\text{-}\mu\text{m}$ WV band BTs over the near global area (45° N – 45° S) for the entire 3 years, as well as that over the northern (0° – 45° N) and southern (0° – 45° S) hemisphere for two different seasons, December–January–February (DJF) and June–July–August (JJA), are shown in Figure 1. The weights were calculated by the cosine of the latitude [12,38,39] and the area were separated for (a) land and (b) ocean to display the land–sea contrast. Overall, the amplitude of the diurnal anomaly of 3-year mean BTs is larger over land than over ocean. The BTs reach the maximum and minimum values over land at 15:00–18:00 LST and 3:00–6:00 LST, respectively. In contrast, the BTs over ocean show maxima and minima at 14:00–16:00 LST and 0:00–3:00 LST, respectively. This indicates that the upper troposphere tends to be more humid in the nighttime (0:00–6:00 LST) and drier in the midafternoon to early evening (14:00–20:00 LST). These results are comparable with previous observational studies [14–16,40]. The diurnal anomalies over the two hemispheres for two different seasons show that the diurnal variation of BTs (UTH) is strong in the summer hemisphere, suggesting its relationship with the active convections. In the study

period, observations for two DJF seasons (2015/16, 2016/17) and three JJA seasons (2015, 2016, and 2017) are available and have been used in the following analysis to present the strong diurnal signals in different seasons. It should be noted that the observations from Meteosat-8, one of the international GEO satellites used in the homogenized WV radiances data, are only available since November 2016. Therefore, the regions near 50° E–80° E measured by Meteosat-8 just have observations for one DJF and one JJA season.

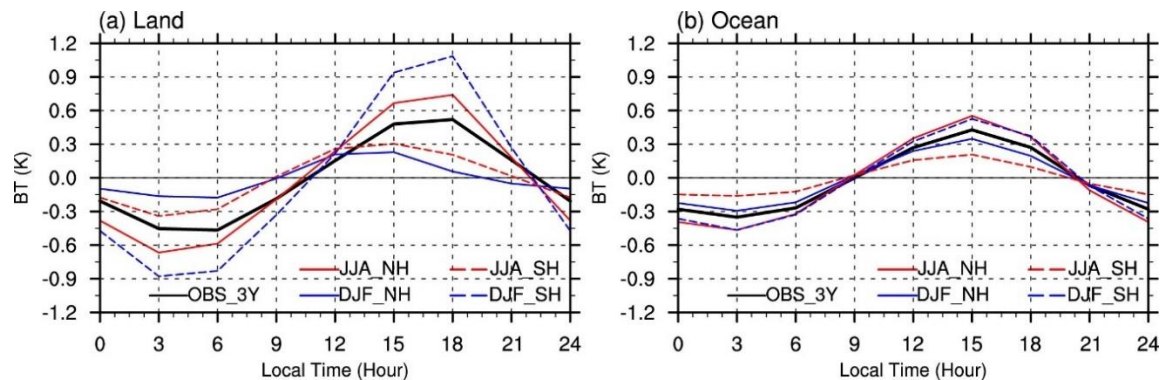


Figure 1. (a) Diurnal anomalies of the observed clear-sky 6.5- μm water vapor (WV) band brightness temperature (BT) averaged over (a) land regions and (b) ocean regions over global area (45° N–45° S) for the entire period of 2015–2017 (black solid line), and over the northern hemisphere (NH; 0°–45° N), and southern hemisphere (SH; 0°–45° S) for two seasons (December–January–February, DJF and June–July–August, JJA).

3.1.2. Observed Global Distribution

Figure 2 shows the geographical distributions of seasonal mean BTs for boreal winter (DJF) and summer (JJA) in 2015–2017. Also shown are the two important components of the diurnal variation of the UTH: the amplitude and the phase derived using first order (24-h) Fourier analysis mentioned in Section 2.3. The results are spatially smoothed to a 2.5° \times 2.5° grid resolution to reduce the influence of mesoscale and microscale disturbance and make the results more clarified. The distributions of observed BTs are continuous throughout the coverage of different satellites, which further indicates that this homogenized WV radiances dataset has good performance in homogeneity and consistency. As indicated by Equation (1), the distribution of seasonal mean BTs is highly related to the distributions of seasonal mean UTH, with colder temperature corresponding to higher WV content in the upper troposphere. The convective regions are thus clearly indicated by the cold BT fields in Figure 2a,b, such as South Africa, the “Marine Continent” of the western Pacific, South America in DJF, and the Central Africa and India monsoon regions in JJA. The movement of the cold BT (high UTH) fields between DJF and JJA is consistent with the seasonal transition of the intertropical convergence zone (ITCZ) and the movement of deep convection centers.

The land–sea contrast for the diurnal variation of UTH is clearly revealed in Figure 2c,d. Larger diurnal amplitudes of UTH are observed over the deep convective regions (high UTH area in Figure 2a,b), especially over convective land regions. In contrast, the diurnal amplitudes are much weaker over non-convective subtropical regions where the warm BT bands are dominant. In general, the UTH peaks earlier over ocean in early night (0:00–3:00 LST) than over land at around late night to early morning (3:00–6:00 LST). The seasonal differences of the diurnal phase of UTH over these convective regions appear to be small over both land and ocean.

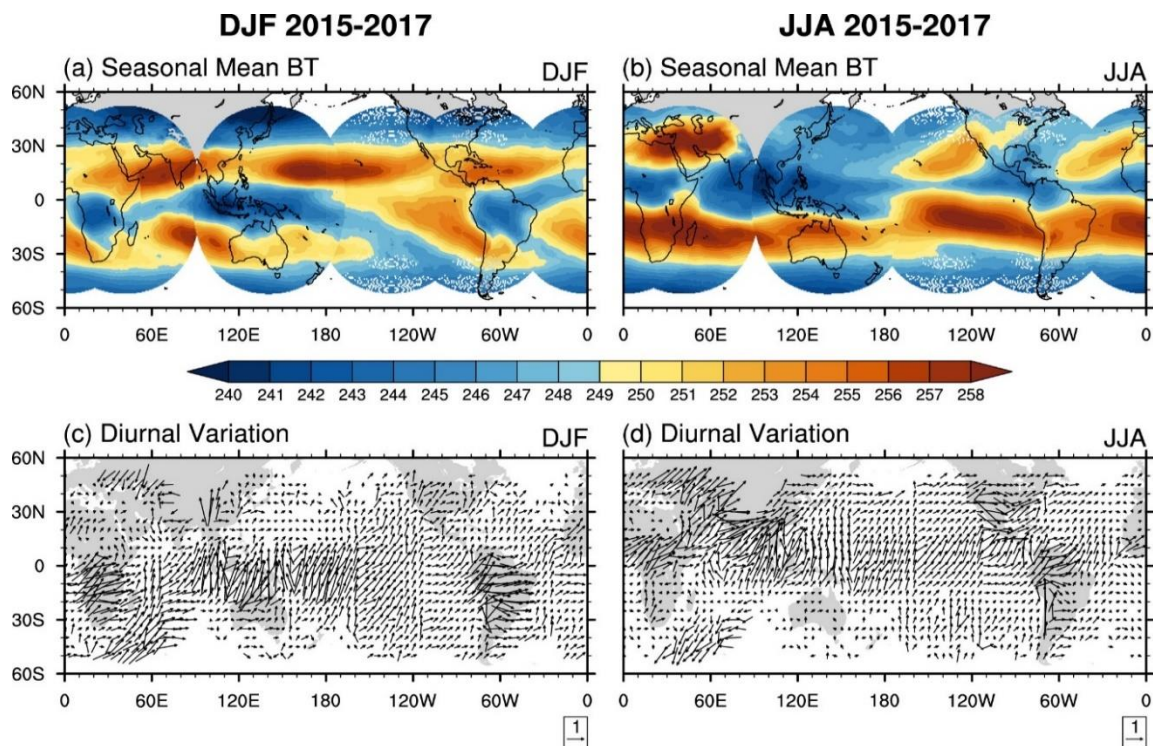


Figure 2. Geographical distributions of (**upper panel**) observed seasonal mean BTs (unit: K) and (**lower panel**) observed diurnal amplitudes of BTs and diurnal phases of UTH for (**left panel**) DJF and (**right panel**) JJA in 2015–2017. The length of the arrow in vector figures denotes the diurnal amplitude (unit: K). The orientation of the arrow with respect to a 24-h clock depicts the diurnal phase (local standard time, LST). For example, arrows pointing upward indicate the UTH peaks at 00:00 LST (midnight). For clarity, results are only shown in every other grid point.

3.2. Comparisons between Observed and Simulated Diurnal Variation

3.2.1. Diurnal Variation of Brightness Temperature Differences

The BT differences (BTDs) are defined as the simulated BTs from reanalysis datasets minus the observed BTs. As inferred from Equation (1), a negative BTD corresponds to a wet UTH bias while a positive BTD indicates a dry UTH bias. The diurnal variation of near global mean BTDs over land and ocean for DJF and JJA are shown in Figure 3. The BTDs are negative at each time step in one composite day, which indicates an overall wet bias in the upper troposphere in all reanalysis datasets. The BTDs typically reach the maximum absolute value near 15:00–18:00 LST over land and 12:00–15:00 LST over ocean, when observed BTs experience a diurnal maximum (Figure 1). This indicates that the reanalysis datasets tend to have larger UTH biases in a drier upper troposphere. Previous studies [41,42] have shown that a dry upper troposphere is usually related to the descending branches of large-scale circulations. Therefore, this may suggest that the large-scale circulation, especially the descending branches, is not well simulated in reanalysis systems.

The BT bias is largest in MERRA-2, about 1 K more negative than other datasets, indicating the wettest upper troposphere in MERRA-2 when compared with the other four reanalysis datasets. Additionally, the BT bias in MERRA-2 is larger in JJA than in DJF, which is not obvious in other reanalysis datasets. In contrast, the JRA55 has a comparable simulation of UTH to observations with the smallest mean BTD of -1.56 K among all reanalysis datasets. According to Equation (1), a BTD of 1 K corresponds to an uncertainty in $\frac{UTH}{\text{BTD}}$ of approximately -0.1 [17,43]. Therefore, if the UTH is 50%, then this BTD in JRA55 can be roughly estimated as a UTH wet bias of 7.8%. Figure 3 also shows that

when compared with the ERA-Interim, the overall UTH simulations in ERA5 have been improved with smaller BTDs in both DJF and JJA seasons and over both land and ocean.

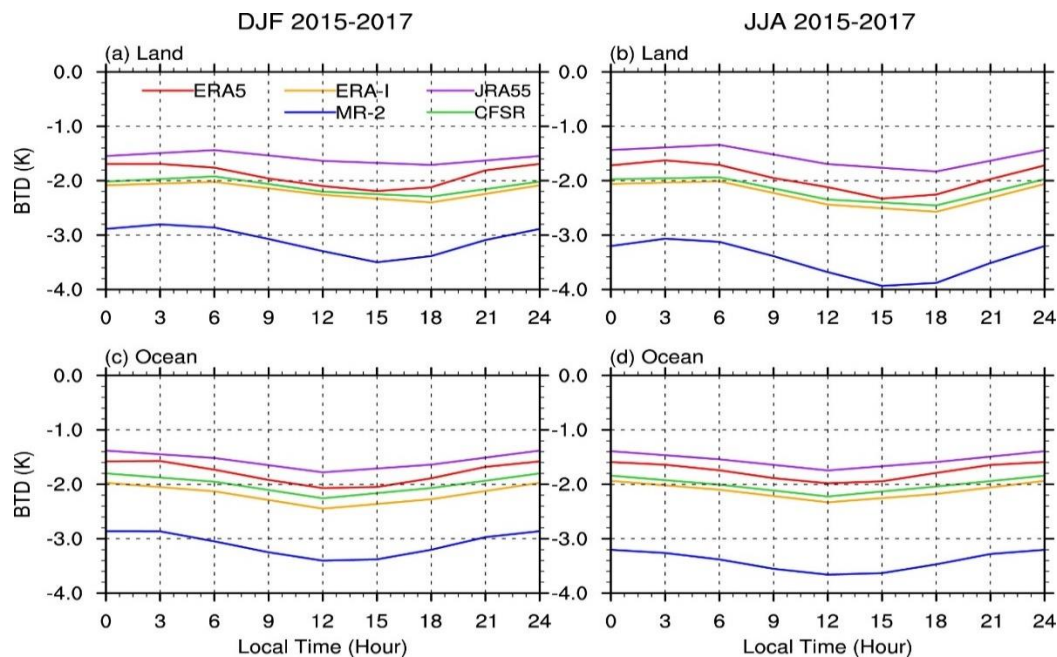


Figure 3. The diurnal variation of the BT differences (BTDs), which are calculated by the simulated BTs in reanalysis datasets minus the observed BTs, over (a,b) land and (c,d) ocean between 45° N and 45° S for (left panel) DJF and (right panel) JJA in 2015–2017.

3.2.2. Diurnal Anomaly

The diurnal anomalies of simulated BTs for area-weighted average over land and ocean for DJF and JJA in 2015–2017 are shown in Figure 4 along with the observations. Overall, all reanalyses can roughly reproduce the day–night contrast of UTH, with the maximum BTs (minimum UTH) found in the late afternoon to early evening and the minimum BTs (maximum UTH) in the nighttime to the early morning. However, differences are clearly shown in both the diurnal amplitude and phase when compared with observed diurnal anomalies. The amplitudes of the diurnal variation are significantly weaker in reanalysis datasets over both land and ocean. In other words, the reanalysis datasets tend to overestimate (underestimate) the moisture content when the upper troposphere has dry (wet) anomalies indicated by the warm (cold) BT anomalies. Furthermore, the LST for the minimum BTs (maximum UTH) in reanalysis datasets lags about 3 h behind the observations, especially over ocean. As a result, the observed global land–sea contrast in the phase of UTH is not well represented in reanalysis datasets.

The discrepancies in different reanalysis datasets are distinct over land. In particular, the diurnal amplitude in MERRA-2 is the smallest compared with other reanalysis datasets over land. The observed diurnal amplitude is larger over global land than over ocean, especially in boreal summer in the study period, while the land–sea contrast of the diurnal amplitude is not obvious in reanalysis datasets. In addition, the observed diurnal amplitude is slightly larger in JJA than in DJF over land in the study period, which is not obvious in the reanalysis datasets either. The seasonal differences of the diurnal variation in both observations and reanalysis are small over ocean. In general, the reanalysis datasets cannot simulate the main characteristic (amplitude and phase) of the diurnal anomaly of near global mean UTH well.

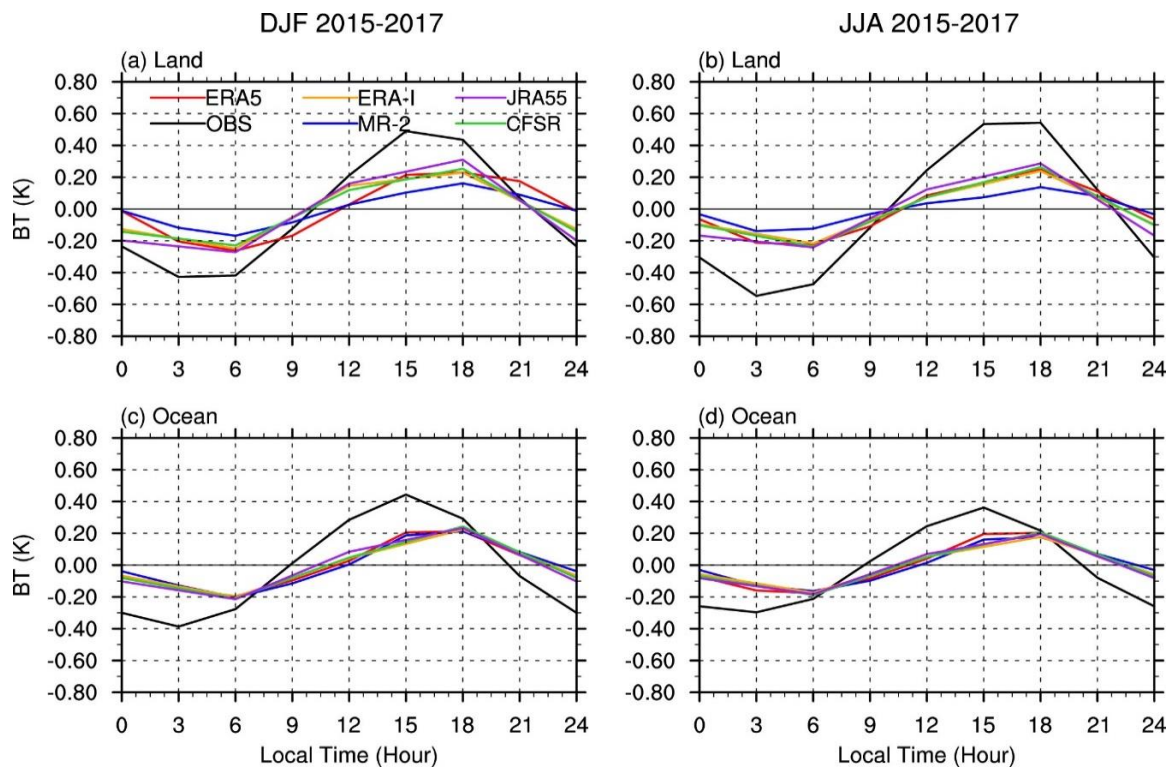


Figure 4. Diurnal anomalies of BTs simulated from ERA5, MERRA-2, ERA-Interim, CFSR, and JRA55 averaged over (a,b) land and (c,d) ocean regions between 45° N and 45° S for (left panel) DJF and (right panel) JJA in 2015–2017. The black lines denote the diurnal anomalies of observed BTs for the same period. The MR-2 is short for MERRA-2.

3.2.3. Global Distribution

The geographical distribution of the diurnal amplitude of BTs and the phase of UTH are also constructed from reanalysis datasets for comparison to satellite observations. Since only ERA5 and MERRA-2 can provide 3-hourly simulated BTs for the daily composite that could be accurately decomposed using Fourier analysis, the following evaluations are mainly focused on these two reanalysis datasets. In addition, the main deficiencies in reanalysis for DJF and JJA are similar, thus only the results for the JJA season are presented.

It is clearly shown in Figure 5 that the diurnal variations in both ERA5 and MERRA-2 are much weaker than the observations (Figure 2c,d) on the global scale. First, the number of grids which have significant diurnal (24-h) signal are smaller in reanalysis datasets, indicated by the lower density of vectors. Second, the diurnal amplitudes of BTs are much smaller when compared with observations. Nevertheless, the two reanalysis datasets could still roughly capture the spatial distribution of the observed diurnal variation of UTH, that is, larger diurnal variation in deep convective regions.

To illustrate the diurnal phase, the histograms of the diurnal phase summarized over land and ocean grids for observations and reanalysis datasets are displayed in the lower panel of Figure 5. Only those grids with statistically significant diurnal (24-h) components were counted. The results clearly show a phase shift in reanalysis data with respect to observations over ocean. The observed maximum UTH over ocean shows a broad peak time from 22:00 LST and mostly occurs around 02:00–03:00 LST, whereas the UTH in ERA5 and MERRA-2 usually experiences a maximum around 04:00–05:00 LST over most of the oceans, which is about 2 h later than observations, and does not show the late evening (~22:00) peak well. The phase differences between observations and ERA5 are relatively small. However, the diurnal phase of UTH over land in MERRA-2 is not well defined, exhibiting a broad range of peak time, from 23:00–12:00, with no obvious dominant single peak.

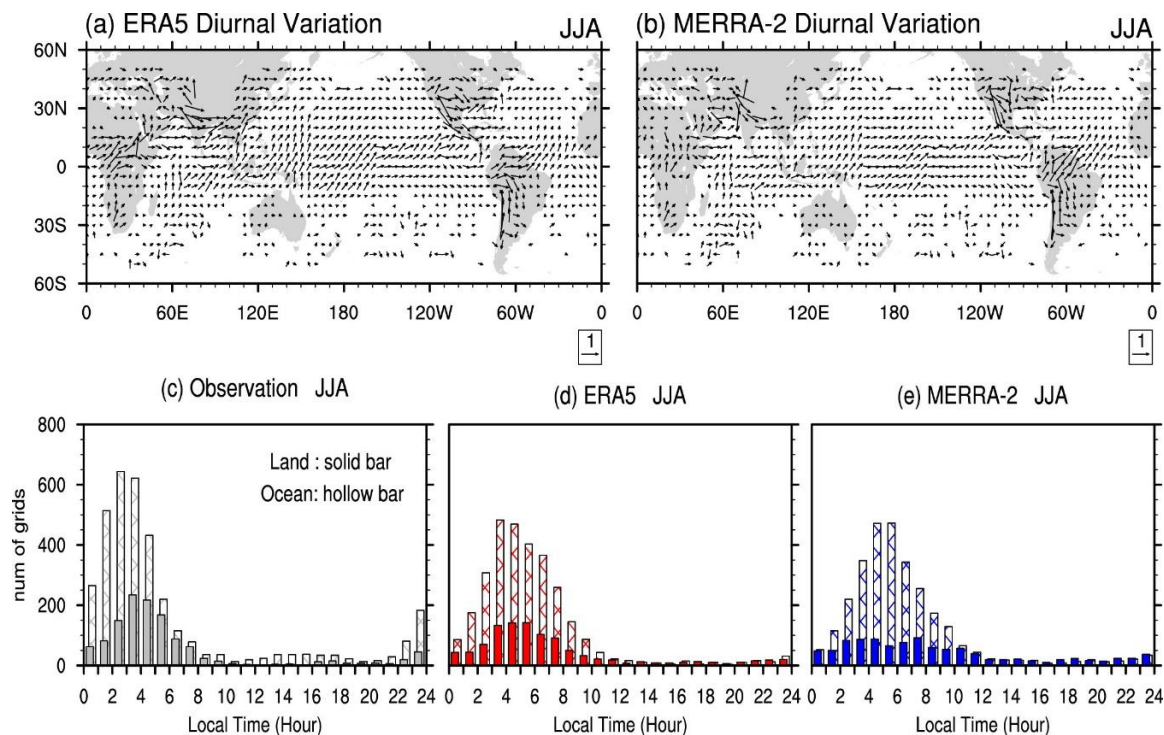


Figure 5. (upper panel) Geographical distributions of diurnal amplitudes of BTs and diurnal phases (peak time) of UTH in (a) ERA5 and (b) MERRA-2 for JJA of 2015–2017. The length of the arrow denotes the diurnal amplitude (unit: K). The orientation of the arrow with respect to a 24-h clock depicts the diurnal phase (local standard time, LST). For example, arrows pointing upward indicate the UTH peaks at 00:00 LST (midnight). For clarity, results are only shown in every other grid point. (lower panel). Histograms of the diurnal phase of UTH for land (solid bar) and ocean (hollow bar) grids from (c) satellite observations, (d) ERA5, and (e) MERRA-2. Only those grids with significant diurnal (24-h) signal were counted.

The quantitative differences of amplitude and phase between the simulated and observed diurnal variations of UTH (simulations minus observations) are provided in Figure 6. For the diurnal amplitude, the ERA5 and MERRA-2 tend to underestimate the diurnal amplitude of BTs by about -0.3 K over much of the oceans. In contrast, the amplitude biases are much larger over convective regions, especially over continental convective regions such as Central Africa, South America, and India. A few studies [14–16] have revealed that the diurnal variation of UTH is highly regulated by deep convections. For example, Chung et al. [14] investigated the relationship between UTH and convective activities over tropical Africa with the Meteosat-8 measurements. They found that deep convections could transport the cloud condensates and WV upward into the upper troposphere during the developing period. These condensates will be detrained into the surrounding environment in the decay period through the cirrus anvil clouds spreading, and then increase the moisture content in the upper troposphere by evaporation/sublimation. As a result, the larger amplitude biases over convective regions suggest that there might be some deficiencies in convection and cloud parameterization schemes in reanalysis models.

For the diurnal phase, a substantial time lag is widely seen, especially over ocean. The peak time of UTH in ERA5 mostly lags observations by about 1.5–2 h, in comparison to 2.5–3 h in MERRA-2 over ocean. This result is similar to the result of Tian et al. [15], who found that the maximum of UTH in Geophysical Fluid Dynamics Laboratory (GFDL) global atmosphere and land model (AM2/LM2) is usually 3 h later than observed. Unlike the amplitude biases, the phase biases are much larger over ocean than over land. Studies [15,44] have argued that the diurnally varying sea surface temperature (SST) is important to the oceanic diurnal phase. Therefore, the SST boundary condition in reanalysis

models might be one possible reason for the larger phase lagging over ocean. Although the UTH in reanalysis datasets generally peaks later than that in observations, there are some exceptions where the UTH peaks earlier than that in observations, such as the north of Arabia, the southern Indian Ocean around 30 °S, and north of South America in MERRA-2 in boreal summer. These regional exceptions might be indicative of some local-scale disturbance that needs more investigation. Furthermore, the limited observations over those regions covered only by Meteosat-8 (between about 50° E–80° E) might also introduce some uncertainties. More investigations will be conducted over these regions once more observations are available.

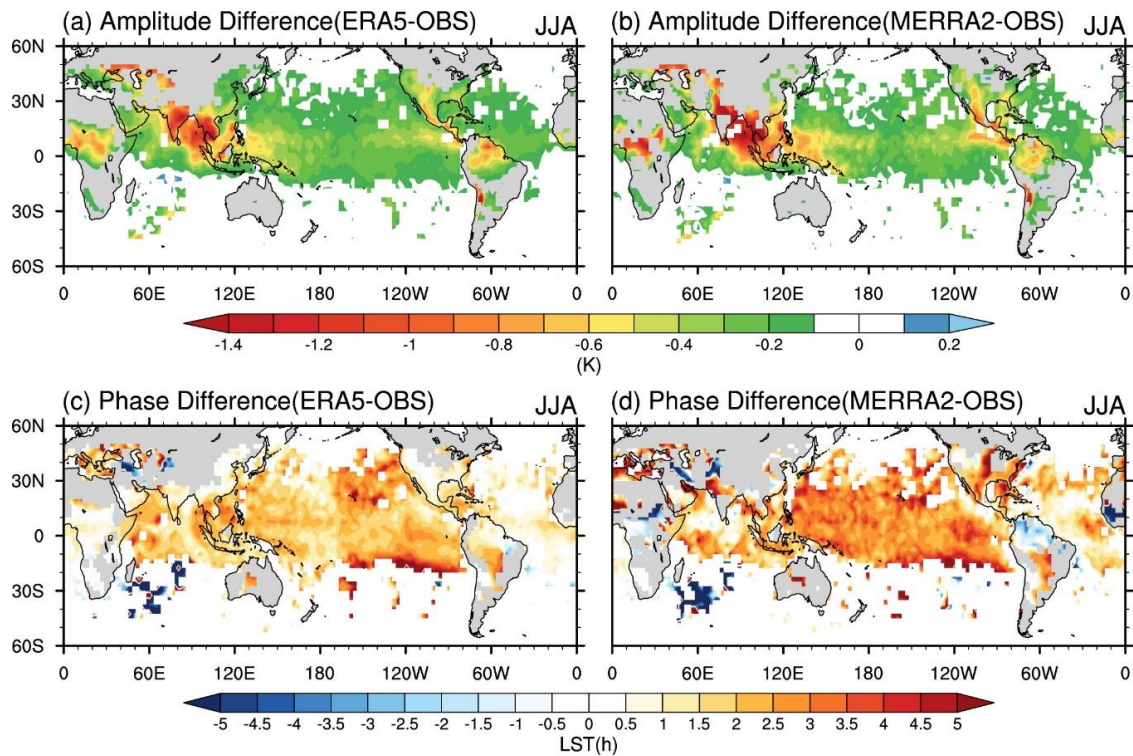


Figure 6. Geographical distributions of differences in (upper panel) diurnal amplitudes of BTs and (lower panel) diurnal phases of UTH between (a,c) ERA5, (b,d) MERRA-2 and observations (reanalysis minus observations) in JJA of 2015–2017. For clarity, results are only shown where the amplitude bias is more than 0.1 K and the phase bias is more than 0.5 h.

4. Discussion

As the observations are clear sky BTs, this study mainly represents the diurnal variation of UTH under clear sky conditions rather than all sky conditions. Although the clear sky sampling might lead to an underestimation of the real moisture environment in the upper troposphere and may also introduce a small bias in the phase of UTH [11,20], the comparison between simulated and observed BT is generally based on the same condition to ensure the differences are not critically affected by the clear-sky sampling bias.

The results from the comparisons are generally consistent over the global scale, such that the reanalysis datasets tend to underestimate the diurnal amplitude and have a later peak time of UTH than observed. However, some geographic differences are seen. For example, a notable exception is over the southern Indian Ocean, where the observations show an afternoon maximum of UTH in boreal summer, whereas ERA5 and MERRA-2 simulations show a morning peak, which is earlier than the observations. These regional differences might be related to local scale convections, topography and limited observations. Longer-time measurements from the Meteosat-8 satellite over the Indian Ocean may help to further examine these differences in the near future.

There are some possible reasons that reanalysis datasets do not capture the major characteristics of the diurnal variation of UTH well. For example, there might be some deficiencies in the convective and cloud parameterization in reanalysis models. The valid observations over convective regions might not be effectively used in the DA systems. Inspired by Kim et al. [36], the simulations of diurnal variations might be improved by increasing the horizontal resolution of models to better represent the local-scale circulations. Although the specific causes are not identified, these evaluation results can provide useful information and important feedback to the model and DA communities for further improving the performance of reanalysis systems.

Recently, with measurements from advanced imagers onboard the new generation of international geostationary weather satellites such as Himawari-8/-9 [45], GOES-16/-17 [46], FengYun-4A [47], and GEO-KOMPSAT-2A, tropospheric moisture information can be obtained with high temporal and spatial resolutions, the WV radiances from the new generation of international GEO weather satellites, once homogenized, can be used to evaluate the diurnal characteristics of both middle tropospheric and upper tropospheric humidity in models and reanalysis systems.

5. Conclusions

This study uses a new homogenized 6.5- μm WV radiances data from international GEO weather satellites to construct the diurnal variation of upper tropospheric moisture and to evaluate the diurnal variations from five modern reanalysis datasets globally between 45° N and 45° S for DJF and JJA of 2015–2017. The main results show that:

1. The diurnal variation of UTH constructed from the new homogenized WV radiances data generally agrees with previous observational studies which were mostly limited to regional scale or short time period [2,11,14–16,20,48]. Larger diurnal variations are observed over the deep convective regions where the mean UTH is high. The land–sea contrast for the diurnal variation of UTH is clearly revealed; that is, the diurnal amplitude is relatively larger over land and the UTH usually peaks earlier over ocean.
2. All five reanalysis datasets show wet biases in the upper troposphere, with the largest bias found in MERRA-2 and smallest bias in JRA55. The wet biases tend to reach the maximum at the time when the UTH reaches the minimum, indicating that reanalysis datasets have slightly more difficulties in simulating the moisture in a drier upper troposphere.
3. Accurately depicting the characteristics in the diurnal variation of UTH is still a challenging task for current reanalysis systems. The diurnal amplitudes of global mean BTs are much weaker in the five reanalysis datasets, and the LST for the minimum BTs (maximum UTH) usually lags about 3 h behind the observations.
4. Both ERA5 and MERRA-2 could roughly capture the larger diurnal variations over deep convective regions. However, the diurnal amplitudes are widely underestimated, especially over convective land regions, which possibly suggests some deficiencies in convection parameterization schemes in reanalysis models. In contrast, the phase biases are relatively larger over the ocean.

Author Contributions: Conceptualization, J.L.; methodology, Y.X., and J.L.; software, Y.X.; validation, Y.X., Z.L., and J.L.; formal analysis, Y.X., Z.L., and J.L.; investigation, Y.X., Z.L., M.M.G., and T.J.S.; resources, J.L.; data curation, Z.L.; writing-original draft preparation, Y.X.; writing-review and editing, J.L., Z.L., M.M.G., T.J.S., and Y.X.; visualization, Y.X.; supervision, J.L.; project administration, Z.L.; funding acquisition, Z.L. All authors have read and agreed to the published version of the manuscript.

Funding: This work is partly supported by NSFC (41775045) and China Scholarship Council (CSC) (Yunheng Xue). It is also partially supported by NOAA's GOES-R series science program NA15NES4320001 (Zhenglong Li, Jun Li, and Mathew M. Gunshor).

Acknowledgments: The new homogenized WV radiance data from international GEO imagers can be obtained by applying the regression coefficients with the Matlab reader (ftp://ftp.ssec.wisc.edu/ABS/zli/GEO_WV_Homogenization_Coeffs/regression_coef_supplemental_materials.tar) to the radiance measurements available from the Data Center at the Space Science and Engineering Center at University of Wisconsin-Madison

(<https://www.ssec.wisc.edu/datacenter/>). The ERA5 and ERA-Interim data are obtained from ECMWF at <https://www.ecmwf.int/en/forecasts/datasets/browse-reanalysis-datasets>. The CFSR and MERRA-2 reanalysis are obtained from <https://rda.ucar.edu> and <https://disc.gsfc.nasa.gov/>, respectively. The JRA55 reanalysis project carried out by JMA is available at <https://rda.ucar.edu/>. The views, opinions and findings contained in this report are those of the authors and should not be construed as an official NOAA or U.S. government position, policy, or decision.

Conflicts of Interest: The authors declare no conflict of interest.

References

- Held, I.M.; Soden, B.J. Water vapor feedback and global warming. *Annu. Rev. Energy Environ.* **2000**, *25*, 441–475. [[CrossRef](#)]
- Chung, E.-S.; Sohn, B.-J.; Schmetz, J. Diurnal variation of outgoing longwave radiation associated with high cloud and UTH changes from Meteosat-5 measurements. *Meteorol. Atmos. Phys.* **2009**, *105*, 109–119. [[CrossRef](#)]
- Allan, R.P. The role of water vapour in Earth's energy flows. *Surv. Geophys.* **2012**, *33*, 557–564. [[CrossRef](#)]
- Houghton, J.T.; Ding, Y.; Griggs, D.J.; Noguer, M.; Van der Linden, P.J.; Dai, X.; Maskell, K.; Johnson, C.A. *Climate Change 2001: The Scientific Basis*; The Press Syndicate of the University of Cambridge: Cambridge, UK, 2001.
- Elliott, W.P.; Gaffen, D.J. On the utility of radiosonde humidity archives for climate studies. *Bull. Am. Meteorol. Soc.* **1991**, *72*, 1507–1520. [[CrossRef](#)]
- Miloshevich, L.M.; Vömel, H.; Whiteman, D.N.; Lesht, B.M.; Schmidlin, F.J.; Russo, F. Absolute accuracy of water vapor measurements from six operational radiosonde types launched during AWEX-G and implications for AIRS validation. *J. Geophys. Res. Atmos.* **2006**, *111*. [[CrossRef](#)]
- Wang, J.; Carlson, D.J.; Parsons, D.B.; Hock, T.F.; Lauritsen, D.; Cole, H.L.; Beierle, K.; Chamberlain, E. Performance of operational radiosonde humidity sensors in direct comparison with a chilled mirror dew-point hygrometer and its climate implication. *Geophys. Res. Lett.* **2003**, *30*. [[CrossRef](#)]
- Davis, S.M.; Hegglin, M.I.; Fujiwara, M.; Dragani, R.; Harada, Y.; Kobayashi, C.; Long, C.; Manney, G.L.; Nash, E.R.; Potter, G.L.; et al. Assessment of upper tropospheric and stratospheric water vapor and ozone in reanalyses as part of S-RIP. *Atmospheric Chem. Phys.* **2017**, *17*, 12743–12778. [[CrossRef](#)]
- Jiang, J.H.; Su, H.; Zhai, C.; Wu, L.; Minschwaner, K.; Molod, A.M.; Tompkins, A.M. An assessment of upper troposphere and lower stratosphere water vapor in MERRA, MERRA2, and ECMWF reanalyses using Aura MLS observations. *J. Geophys. Res. Atmos.* **2015**, *120*, 11468–11485. [[CrossRef](#)]
- Dessler, A.E.; Davis, S.M. Trends in tropospheric humidity from reanalysis systems. *J. Geophys. Res. Atmos.* **2010**, *115*. [[CrossRef](#)]
- Chung, E.-S.; Soden, B.J.; Sohn, B.J.; Schmetz, J. An assessment of the diurnal variation of upper tropospheric humidity in reanalysis data sets. *J. Geophys. Res. Atmos.* **2013**, *118*, 3425–3430. [[CrossRef](#)]
- Iacono, M.J.; Delamere, J.S.; Mlawer, E.J.; Clough, S.A. Evaluation of upper tropospheric water vapor in the NCAR Community Climate Model (CCM3) using modeled and observed HIRS radiances. *J. Geophys. Res. Atmos.* **2003**, *108*, ACL 1-1–ACL 1-19. [[CrossRef](#)]
- Yang, G.-Y.; Slingo, J. The Diurnal Cycle in the Tropics. *Mon. Weather Rev.* **2001**, *129*, 784–801. [[CrossRef](#)]
- Chung, E.S.; Sohn, B.J.; Schmetz, J.; Koenig, M. Diurnal variation of upper tropospheric humidity and its relations to convective activities over tropical Africa. *Atmos. Chem. Phys.* **2007**, *7*, 2489–2502. [[CrossRef](#)]
- Tian, B.; Soden, B.J.; Wu, X. Diurnal cycle of convection, clouds, and water vapor in the tropical upper troposphere: Satellites versus a general circulation model. *J. Geophys. Res. Atmos.* **2004**, *109*. [[CrossRef](#)]
- Soden, B.J. The diurnal cycle of convection, clouds, and water vapor in the tropical upper troposphere. *Geophys. Res. Lett.* **2000**, *27*, 2173–2176. [[CrossRef](#)]
- Soden, B.J.; Bretherton, F.P. Upper tropospheric relative humidity from the GOES 6.7 μm channel: Method and climatology for July 1987. *J. Geophys. Res.* **1993**, *98*, 16669–16688. [[CrossRef](#)]
- Di, D.; Ai, Y.; Li, J.; Shi, W.; Lu, N. Geostationary satellite-based 6.7 μm band best water vapor information layer analysis over the Tibetan Plateau. *J. Geophys. Res. Atmos.* **2016**, *121*, 4600–4613. [[CrossRef](#)]
- Li, Z.; Li, J.; Gunshor, M.; Moeller, S.-C.; Schmit, T.J.; Yu, F.; McCarty, W. Homogenized Water Vapor Absorption Band Radiances From International Geostationary Satellites. *Geophys. Res. Lett.* **2019**, *46*, 10599–10608. [[CrossRef](#)]

20. Kottayil, A.; John, V.O.; Buehler, S.A.; Mohanakumar, K. Evaluating the Diurnal Cycle of Upper Tropospheric Humidity in Two Different Climate Models Using Satellite Observations. *Remote Sens.* **2016**, *8*, 325. [[CrossRef](#)]
21. Menzel, W.P.; Schmit, T.J.; Zhang, P.; Li, J. Satellite-based atmospheric infrared sounder development and applications. *Bull. Am. Meteorol. Soc.* **2018**, *99*, 583–603. [[CrossRef](#)]
22. Dee, D.P.; Uppala, S.M.; Simmons, A.J.; Berrisford, P.; Poli, P.; Kobayashi, S.; Andrae, U.; Balmaseda, M.A.; Balsamo, G.; Bauer, P. The ERA-Interim reanalysis: Configuration and performance of the data assimilation system. *Q. J. R. Meteorol. Soc.* **2011**, *137*, 553–597. [[CrossRef](#)]
23. Kobayashi, S.; Ota, Y.; Harada, Y.; Ebata, A.; Moriya, M.; Onoda, H.; Onogi, K.; Kamahori, H.; Kobayashi, C.; Endo, H. The JRA-55 reanalysis: General specifications and basic characteristics. *J. Meteorol. Soc. Jpn. Ser. II* **2015**, *93*, 5–48. [[CrossRef](#)]
24. Gelaro, R.; McCarty, W.; Suárez, M.J.; Todling, R.; Molod, A.; Takacs, L.; Randles, C.A.; Darmenov, A.; Bosilovich, M.G.; Reichle, R. The modern-era retrospective analysis for research and applications, version 2 (MERRA-2). *J. Clim.* **2017**, *30*, 5419–5454. [[CrossRef](#)] [[PubMed](#)]
25. Hersbach, H.; Dee, D. ERA5 reanalysis is in production. *ECMWF Newsl.* **2016**, *147*, 5–6.
26. Saha, S.; Moorthi, S.; Wu, X.; Wang, J.; Nadiga, S.; Tripp, P.; Behringer, D.; Hou, Y.-T.; Chuang, H.; Iredell, M.; et al. The NCEP Climate Forecast System Version 2. *J. Clim.* **2013**, *27*, 2185–2208. [[CrossRef](#)]
27. Jiang, X.; Li, J.; Li, Z.; Xue, Y.; Di, D.; Wang, P.; Li, J. Evaluation of Environmental Moisture from NWP Models with Measurements from Advanced Geostationary Satellite Imager—A Case Study. *Remote Sens.* **2020**, *12*, 670. [[CrossRef](#)]
28. Han, Y. *JCSDA Community Radiative Transfer Model (CRTM): Version 1*; National Oceanic and Atmospheric Administration: Washington, DC, USA, 2006.
29. Di, D.; Li, J.; Han, W.; Bai, W.; Wu, C.; Menzel, W.P. Enhancing the Fast Radiative Transfer Model for FengYun-4 GIIRS by Using Local Training Profiles. *J. Geophys. Res. Atmos.* **2018**, *123*, 12583–12596. [[CrossRef](#)]
30. Ding, S.; Yang, P.; Weng, F.; Liu, Q.; Han, Y.; Van Delst, P.; Li, J.; Baum, B. Validation of the community radiative transfer model. *J. Quant. Spectrosc. Radiat. Transf.* **2011**, *112*, 1050–1064. [[CrossRef](#)]
31. Saunders, R.; Rayer, P.; Brunel, P.; Von Engeln, A.; Bormann, N.; Strow, L.; Hannon, S.; Heilliette, S.; Liu, X.; Miskolczi, F.; et al. A comparison of radiative transfer models for simulating Atmospheric Infrared Sounder (AIRS) radiances. *J. Geophys. Res. Atmos.* **2007**, *112*. [[CrossRef](#)]
32. Clough, S.A.; Iacono, M.J.; Moncet, J.-L. Line-by-line calculations of atmospheric fluxes and cooling rates: Application to water vapor. *J. Geophys. Res. Atmos.* **1992**, *97*, 15761–15785. [[CrossRef](#)]
33. Taylor, P.C. Tropical Outgoing Longwave Radiation and Longwave Cloud Forcing Diurnal Cycles from CERES. *J. Atmos. Sci.* **2012**, *69*, 3652–3669. [[CrossRef](#)]
34. Lindfors, A.V.; Mackenzie, I.A.; Tett, S.F.B.; Shi, L. Climatological Diurnal Cycles in Clear-Sky Brightness Temperatures from the High-Resolution Infrared Radiation Sounder (HIRS). *J. Atmos. Ocean. Technol.* **2011**, *28*, 1199–1205. [[CrossRef](#)]
35. Lee, M.-I.; Schubert, S.D.; Suarez, M.J.; Bell, T.L.; Kim, K.-M. Diurnal cycle of precipitation in the NASA Seasonal to Interannual Prediction Project atmospheric general circulation model. *J. Geophys. Res. Atmos.* **2007**, *112*. [[CrossRef](#)]
36. Kim, H.; Lee, M.-I.; Cha, D.-H.; Lim, Y.-K.; Putman, W.M. Improved representation of the diurnal variation of warm season precipitation by an atmospheric general circulation model at a 10 km horizontal resolution. *Clim. Dyn.* **2019**, *53*, 6523–6542. [[CrossRef](#)]
37. Iitterly, K.F.; Taylor, P.C. Evaluation of the Tropical TOA Flux Diurnal Cycle in MERRA and ERA-Interim Retrospective Analyses. *J. Clim.* **2014**, *27*, 4781–4796. [[CrossRef](#)]
38. Lavers, D.A.; Ralph, F.M.; Waliser, D.E.; Gershunov, A.; Dettinger, M.D. Climate change intensification of horizontal water vapor transport in CMIP5. *Geophys. Res. Lett.* **2015**, *42*, 5617–5625. [[CrossRef](#)]
39. Xue, Y.; Li, J.; Menzel, W.P.; Borbas, E.; Ho, S.-P.; Li, Z.; Li, J. Characteristics of Satellite Sampling Errors in Total Precipitable Water from SSMIS, HIRS, and COSMIC Observations. *J. Geophys. Res. Atmos.* **2019**, *124*, 6966–6981. [[CrossRef](#)]
40. Udelhofen, P.M.; Hartmann, D.L. Influence of tropical cloud systems on the relative humidity in the upper troposphere. *J. Geophys. Res. Atmos.* **1995**, *100*, 7423–7440. [[CrossRef](#)]
41. Van de Berg, L.; Pyomjamsri, A.; Schmetz, J. Monthly mean upper tropospheric humidities in cloud-free areas from meteosat observations. *Int. J. Climatol.* **1991**, *11*, 819–826. [[CrossRef](#)]

42. Shi, L.; Schreck, C.J.; Schröder, M. Assessing the Pattern Differences between Satellite-Observed Upper Tropospheric Humidity and Total Column Water Vapor during Major El Niño Events. *Remote Sens.* **2018**, *10*, 1188. [[CrossRef](#)]
43. Soden, B.J.; Bretherton, F.P. Interpretation of TOVS water vapor radiances in terms of layer-average relative humidities: Method and climatology for the upper, middle, and lower troposphere. *J. Geophys. Res. Atmos.* **1996**, *101*, 9333–9343. [[CrossRef](#)]
44. Chen, S.S.; Houze, R.A., Jr. Diurnal variation and life-cycle of deep convective systems over the tropical Pacific warm pool. *Q. J. R. Meteorol. Soc.* **1997**, *123*, 357–388. [[CrossRef](#)]
45. Bessho, K.; Date, K.; Hayashi, M.; Ikeda, A.; Imai, T.; Inoue, H.; Kumagai, Y.; Miyakawa, T.; Murata, H.; Ohno, T.; et al. An Introduction to Himawari-8/9—Japan’s New-Generation Geostationary Meteorological Satellites. *J. Meteorol. Soc. Jpn. Ser. II* **2016**, *94*, 151–183. [[CrossRef](#)]
46. Schmit, T.J.; Gunshor, M.M.; Menzel, W.P.; Gurka, J.J.; Li, J.; Bachmeier, A.S. Introducing the next-generation Advanced Baseline Imager on GOES-R. *Bull. Am. Meteorol. Soc.* **2005**, *86*, 1079–1096. [[CrossRef](#)]
47. Yang, J.; Zhang, Z.; Wei, C.; Lu, F.; Guo, Q. Introducing the New Generation of Chinese Geostationary Weather Satellites, Fengyun-4. *Bull. Am. Meteorol. Soc.* **2016**, *98*, 1637–1658. [[CrossRef](#)]
48. Zhang, Y.; Klein, S.A.; Liu, C.; Tian, B.; Marchand, R.T.; Haynes, J.M.; McCoy, R.B.; Zhang, Y.; Ackerman, T.P. On the diurnal cycle of deep convection, high-level cloud, and upper troposphere water vapor in the Multiscale Modeling Framework. *J. Geophys. Res. Atmos.* **2008**, *113*. [[CrossRef](#)]



© 2020 by the authors. Licensee MDPI, Basel, Switzerland. This article is an open access article distributed under the terms and conditions of the Creative Commons Attribution (CC BY) license (<http://creativecommons.org/licenses/by/4.0/>).